

Highlights from the Telescope Array Experiment

Jihyun Kim^{a,*} for the Telescope Array Collaboration

^a*High Energy Astrophysics Institute and Department of Physics and Astronomy, University of Utah
Salt Lake City, Utah 84112-0830, USA*

E-mail: jihyun@cosmic.utah.edu

The Telescope Array (TA) is the largest ultra-high energy cosmic ray (UHECR) observatory in the Northern Hemisphere. Together with the TA Low Energy Extension (TALE), TA×4, and TALE infill detector, the TA measures the properties of UHECR-induced extensive air showers (EAS) in the energy region from 10^{15} eV to over 10^{20} eV. Each of these uses a hybrid system with an array of scintillators to sample the footprint of the EAS at the Earth's surface along with telescopes that measure the fluorescence and Cherenkov light from the EAS. The statistics at the highest energies are being enhanced with the TA×4 detector, half completed but still under construction, which will quadruple the surface detector area with telescopes. The TALE infill surface detectors were recently deployed to further lower the hybrid energy threshold of TALE. We present the status of the experiment and recent results on the energy spectrum, mass composition, and anisotropy, including new features in the energy spectrum at about $10^{19.2}$ eV and in the UHECR arrival direction anisotropy.

38th International Cosmic Ray Conference (ICRC2023)
26 July - 3 August, 2023
Nagoya, Japan



*Speaker

1. Introduction

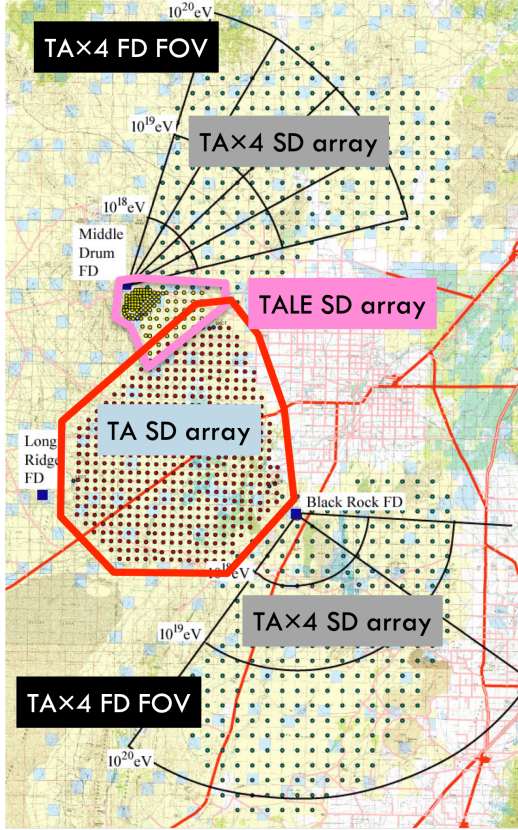


Figure 1: Map of the Telescope Array experiment together with the extensions. The red border line indicates the Telescope Array (TA), and the pink one represents the low energy extension, Telescope Array Low Energy Extension (TALE). The fourfold extension of TA, TA×4, is located north and south of the main TA array. All the TA projects employ a hybrid technique to observe extensive air showers induced by primary ultra-high energy particles striking the Earth’s atmosphere.

As briefly described above, TA employs a hybrid technique using surface and fluorescence detectors (SDs, FDs) [8, 9]. A total of 507 SDs are laid out with 1.2 km spacing on a square grid over approximately 700 km² area, as indicated with the red line in Figure 1. Three FD stations are sited at the apices of a triangle with each station, viewing between 3°–31° in elevation over the airspace above the SD array. A total of 38 fluorescence telescopes are distributed over these three stations to measure the ultraviolet light emitted as the extensive air shower traverses the atmosphere.

TALE is designed to observe cosmic rays with energies from $\sim 10^{18}$ eV down to $\sim 10^{15}$ eV [10]. The TALE FD station is located next to the TA Middle Drum FD. The pink line in Figure 1 indicates

The Telescope Array (TA) is the largest ultra-high energy cosmic ray (UHECR) observatory in the Northern Hemisphere. It is located in Delta, Utah, USA, at about 1400 m above sea level, which is perfect for observing extensive air showers (EAS) induced by UHECRs. Together with the TA Low Energy Extension (TALE) and TA×4 expansion, TA measures the properties of the EAS by employing a hybrid technique using arrays of scintillator detectors that sample the footprint of the EAS at the Earth’s surface along with imaging telescopes that measure the fluorescence and Cherenkov light from the EAS.

The scientific objectives of TA are to understand the origin and nature of UHECRs by studying their energy spectrum, mass composition, and anisotropy. In addition, we are making efforts to understand the physics of hadronic interactions in the ultra-high energy (UHE) regime beyond the energy reach by terrestrial accelerators. We also build a bridge to multi-messenger astrophysics, involving searches for high energy photons, neutrinos, and dark matter. We are also engaged in interdisciplinary studies including the study of thunderstorms, terrestrial gamma-ray flash as well as imaging of meteoroids. Furthermore, the TA experiment offers opportunities to utilize the TA sites as a test facility for the development of next-generation UHECR experiments [1–7].

Figure 1 shows the map of the Telescope Array experiment together with the extensions.

TALE's detection area. They comprise 10 telescopes observing 31° – 59° in elevation directly above the view of TA Middle Drum FD. A total of 80 TALE SDs are deployed with 400 to 600 m spacing for hybrid as well as stand-alone measurements.

The combination of TA and TA×4 aims to extend the observation area to about 3000 km^2 [11] in order to enhance significantly our data sample at the highest energies required to identify the origin of UHECR. TA×4 SD array includes 500 new SDs with 2.08 km spacing located on two square grids, one to the north and the other to the south of the original TA array. The extension is focused on the collection of UHECR showers with energies greater than $3 \times 10^{19} \text{ eV}$, so we are able to reduce the cost by a factor of three by increasing the spacing by a factor of $\sqrt{3}$ to 2.08 km. As of 2023, 257 out of 500 SDs are deployed and operational in conjunction with 12 new TA×4 fluorescence telescopes for hybrid measurement. The first deployment increased the SD observation area by $\sim 1000 \text{ km}^2$.

Under the Telescope Array Collaboration, which includes the main TA, TALE, and TA×4, we have conducted observation of cosmic rays spanning the energy range 10^{15} – 10^{21} eV in order to study the origin and nature of cosmic rays. In this conference, TA presents the experiment's current status and recent results related to the energy spectrum, mass composition, and anisotropy. This paper is organized as follows. In Section 2, spectrum measurements by the TA, TALE, and TA×4 are presented, including results from studies of systematic effect on the energy scale. Section 3 presents the latest mass composition analysis using TALE FD monocular and hybrid data, along with ultra-high energy photon searches in TA SD data using a neural network classifier for protons and photons. In Section 4, we update the anisotropy analysis results using the most up-to-date TA SD data. Section 5 covers collaborative efforts of joint working groups for mass composition, anisotropy search, and interdisciplinary research. Finally, Section 6 presents a summary of these discussions.

2. Energy Spectrum

In this Section, we provide updates on the energy spectrum measurements conducted by the main TA, the TALE, and also the TA×4 expansion. The foundation of our analyses relies on the Monte Carlo simulations (MC) using the CORSIKA program [12]. These simulations are used to evaluate our detector performance, reconstruction resolutions, and exposure calculation, ultimately leading to the calculation of energy spectra.

We analyze 14 years of TA SD data. The detectors are estimated to have 20% energy and 1.4° angular resolutions at energies greater than $10^{19.0} \text{ eV}$. Figure 2 shows the measured TA energy spectrum and a comparison of the spectrum between high- and low-declination bands. The left panel shows the energy spectrum acquired from the 14 years of TA SD data with the selection criteria described in [13]. The black points with error bars indicate the data and the black solid line represents a fit to a broken power law with two floating breaks. The first break, usually referred to as the ankle feature, appears at $E_{\text{ankle}} = 10^{18.68 \pm 0.01} \text{ eV}$ with spectral indices of $p_1 = -3.27 \pm 0.02$ before and $p_2 = -2.69 \pm 0.02$ after the ankle. The second break, the cutoff feature, is obtained at $E_{\text{cutoff}} = 10^{19.78 \pm 0.04} \text{ eV}$ with a spectral index of $p_3 = -4.47 \pm 0.41$ after the cutoff.

The right panel of Figure 2 shows differences in the cutoff energies depending on the declination. The suppression occurs at $E = 10^{19.65 \pm 0.03} \text{ eV}$ and $E = 10^{19.84 \pm 0.02} \text{ eV}$ for the lower declination

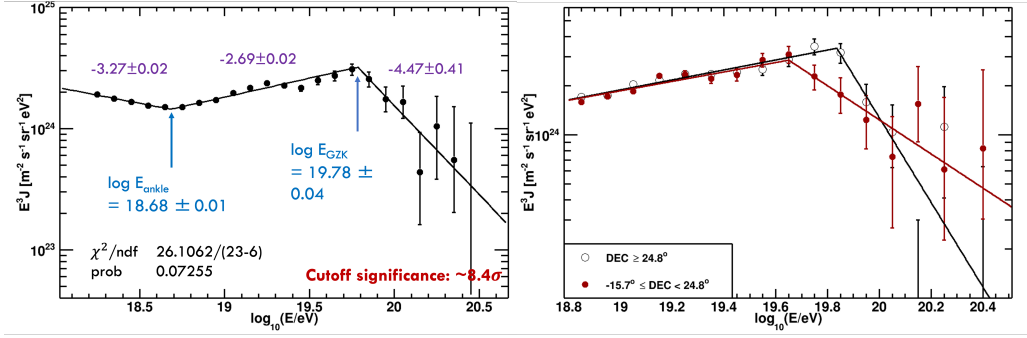


Figure 2: Energy spectrum using 14-year TA SD data and declination dependence in cutoff energies. **Left:** The black dots with error bars indicate the data and the black solid line represents a fit to the broken power law having two breaks, where p_1 , p_2 , and p_3 are the spectral indices before, between, and after the break points of E_{ankle} and E_{cutoff} , respectively. **Right:** The red dots indicates the data in the lower declination band ($-15.7^\circ \leq \delta < 24.8^\circ$) in the TA's field of view overlaid with the red fitting line. The black open circles shows the data in the higher declination range ($\delta \geq 24.8^\circ$) overlaid with its black fitting result.

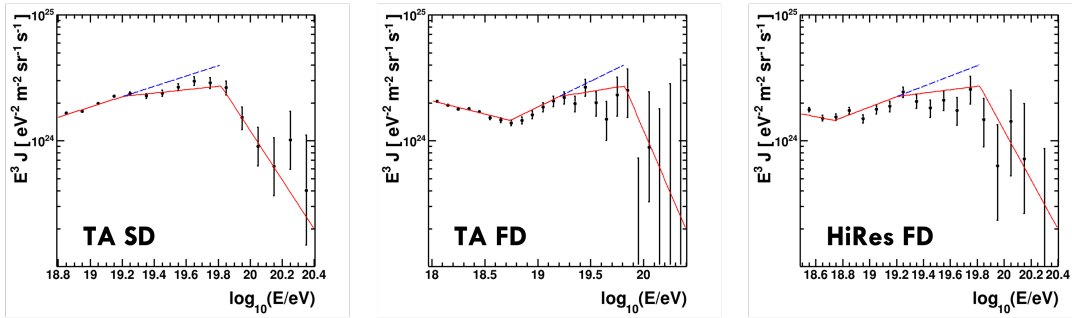


Figure 3: Softening spectral feature in 14-year TA SD data. The black points with error bars represent the datasets and the red solid lines indicate fits to the broken power law having three breaks.

($-15.7^\circ \leq \delta < 24.8^\circ$) and the higher declination ($\delta \geq 24.8^\circ$) bands in the TA's field of view, respectively. The local significance of the difference in cutoff energies is calculated to be 4.8σ , and the global significance of having such a significant difference by chance is estimated to be 4.4σ . We searched for instrumental causes for this cutoff energy difference, but none have been found. This difference is likely astrophysical in nature.

We also observe the softening feature in the energy range from 10^{19} eV to $10^{19.5}$ eV, which was found by the Pierre Auger Observatory (Auger) [14]. Figure 3 shows the softening feature observed in the northern hemisphere by using TA SD, TA FD, and HiRes FD data. The joint fit of the broken power law gives three breaks. The softening feature is observed at $E = 10^{19.20 \pm 0.03}$ eV in the northern hemisphere data with a statistical significance of 6.5σ . This break is higher than $E = 10^{19.11 \pm 0.03}$ observed by Auger. The energies of the softening feature observed by TA and Auger agree at the 1.2σ level after rescaling by 9% in energy. Note that the TA FD observation period was removed from the TA SD spectrum measurement to ensure statistical independence.

We revisit the energy spectrum calculation by adopting the constant-intensity-cut (CIC) reconstruction method [15], which is used for Auger's analysis, in order to explore possible systematic differences between TA and Auger's energy spectrum measurements. In Figure 4, the black points

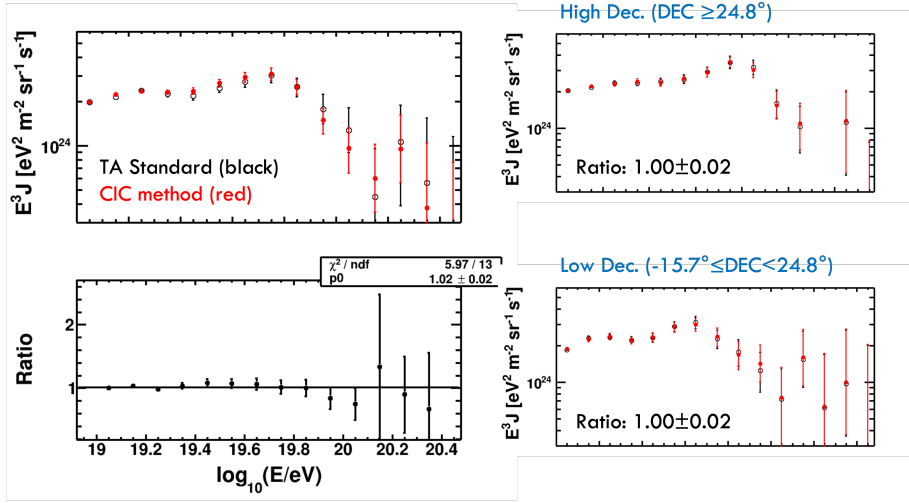


Figure 4: Comparison of energy spectra obtained from the standard method and the CIC method. The black open circles indicate the energy spectrum obtained using the standard method, while the red dots represent the energy spectrum obtained using the CIC method. The results show consistency within a 2%. On the right side, similar comparisons for both high and low declination are presented, and the results remain consistent.

indicate the energy spectrum obtained by the standard MC-based method, and the red points represent that obtained by the CIC method. It shows that they are consistent within 2%. We also perform the same comparisons for the high- and low-declination regions of the sky. The results are consistent, which is further indication that the declination dependence is not a systematic difference.

We conduct systematic studies to assess the effects on the energy scale in energy spectra [16]. This effort is part of our ongoing work to understand the differences between the energy spectra of the TA and Auger. We evaluate the systematic deviations in energy scales within the energy spectrum, originating from differences in atmospheric fluorescence yield and missing energy estimation. By adopting AirFly’s fluorescence yield and Auger’s missing energy estimation, we observe a shift in the scale factor between FD and SD in TA data from 1.27 to 1.35. With this adjusted scale factor, we recalculate the energy spectrum using 14 years of TA SD data, employing both the standard and the CIC methods.

Figure 5 displays the energy spectra obtained by TA and Auger alongside the results of the systematic effect study. Significantly, the energy scale offset, which was approximately +9% in the energies below $10^{19.5}$ eV, is reduced to about +1% when we adopt the same energy assignments arising from the fluorescence yield and invisible energy models. This reduction resulted from the utilization of the AirFly model and Auger’s missing energy estimates, which differed from the standard TA values by approximately -14% and +7% off, respectively. However, persistent differences at higher energies suggest that these differences are independent of TA-Augur FD analysis differences. Again, both the standard method, represented by blue triangles, and the CIC method, represented by red dots, yield consistent energy spectra.

Figure 6 shows energy spectra using TALE FD monocular and hybrid data [17, 18]. The spectra of cosmic rays in the energy range of $10^{15.3}$ – $10^{18.3}$ eV collected by the TALE FD are shown along

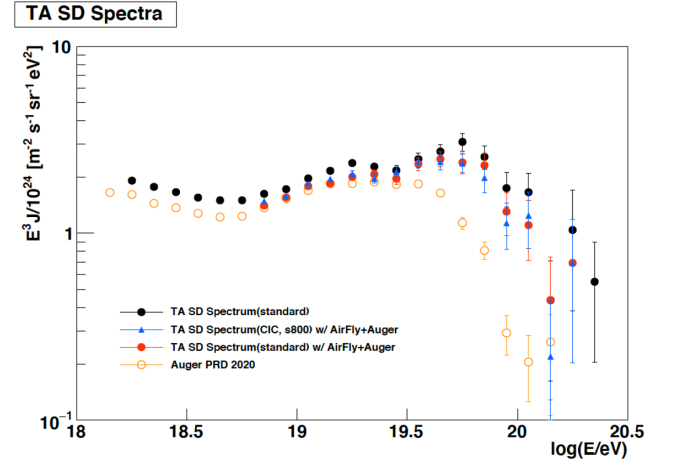


Figure 5: Systematic effects on the energy scale in 14-year TA SD data. The black points indicate the spectrum obtained using 14 years of TA SD data analyzed using the standard TA fluorescence yield and missing energy corrections, while the orange open circles show the Auger results [14]. The TA energy spectra obtained by adopting AirFly’s fluorescence yield and Auger’s missing energy estimation are shown with the red points (using the standard TA MC-based method) and the blue triangles (using the CIC method), respectively.

with the broken power law fits with two breaks. The updated results using TALE FD data collected over a period of approximately 8 years and its broken power law fit are shown with the magenta squares and the blue line on the left panel, respectively. We present the previous measurement of TALE FD data with the black squares and its broken power law fit with the magenta line on the same panel [10]. The parameters to the broken power law fit to the TALE spectra are summarized in the figure. Note that this analysis uses the EPOS-LHC hadronic model while the previous analysis used QGSJetII-03. Therefore, the energy scale has changed overall compared to the previous result.

The preliminary result of the energy spectrum, using TALE hybrid data collected for around 1.5 years, is presented with the black dots on the right panel of Figure 6. This analysis uses the QGSJetII-04 hadronic interaction model. The result is consistent with the previous FD monocular result [10], which is marked with the blue open squares in the figure (the same as the black squares on the left panel). Further analyses with more statistics, as well as with different hadronic interaction models, are ongoing.

As reviewed in Section 1, just over half of the planned TA×4 SDs have been successfully deployed and are operational. We measure the energy spectrum using 3-year TA×4 SD events with energy greater than $10^{19.5}$ eV, where we have reasonably good trigger efficiency [19]. The left panel of Figure 7 shows the measured TA×4 SD energy spectrum along with the result of a fit to a broken power law function. The cutoff appears at $10^{19.85}$ eV, and spectral indices are summarized in the figure. The significance of the cutoff is estimated to be around 2.8σ . Note that the overall spectrum is consistent with the TA SD measurements shown with the gray squares. The right panel of Figure 7 shows the combined energy spectrum using 14 years of TA SD data and 3 years of TA×4 SD data.

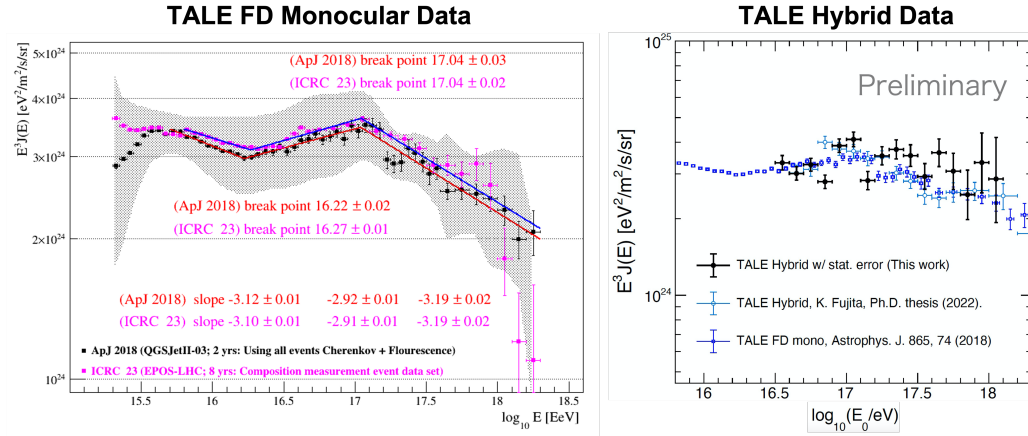


Figure 6: Energy spectra measured by the TALE FD in monocular and hybrid modes. **Left:** The cosmic ray spectra measured by the TALE FD are shown, along with the broken power law fits with two breaks [17]. The magenta squares indicate the updated 8 years of TALE FD data using the EPOS-LHC hadronic model, while the black squares represent the previous data using QGSJetII-03 [10]. The blue and red lines depict the broken power law fits for the updated and previous measurements, respectively. The fit parameters are summarized in the figure. **Right:** The cosmic ray spectra measured by the TALE hybrid mode are displayed here [18]. The black points represent TALE hybrid data collected for approximately 1.5 years, while blue open squares are the previous TALE FD data [10], which are the same as the black squares in the left panel. The results are consistent with the previous FD monocular result.

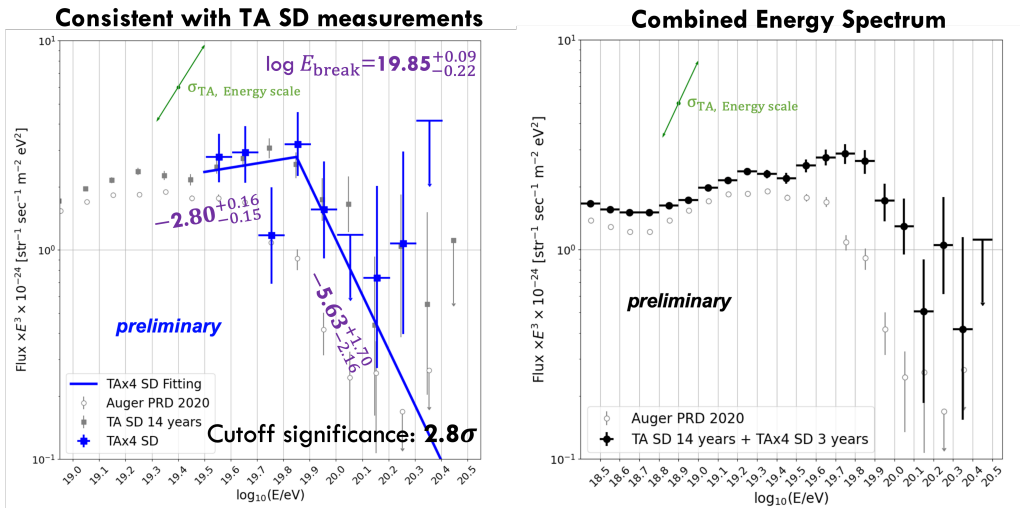


Figure 7: Energy spectrum measured by the TA \times 4 SD and the combined energy spectrum with TA SD. **Left:** The energy spectrum measured by the TA \times 4 SD over three years is presented with the blue squares representing the data and a blue line indicating the broken power law fit [19]. We have included the TA SD energy spectrum using the filled gray squares and the Auger energy spectrum [14] with the gray open circles for comparison. The green arrow denotes the systematic uncertainty arising from the 21% uncertainty in the energy scale, which is nearly independent of energy [20]. **Right:** The combined energy spectrum of 14 years of TA SD data and 3 years of TA \times 4 SD data is shown with the black dots together with Auger's data [14].

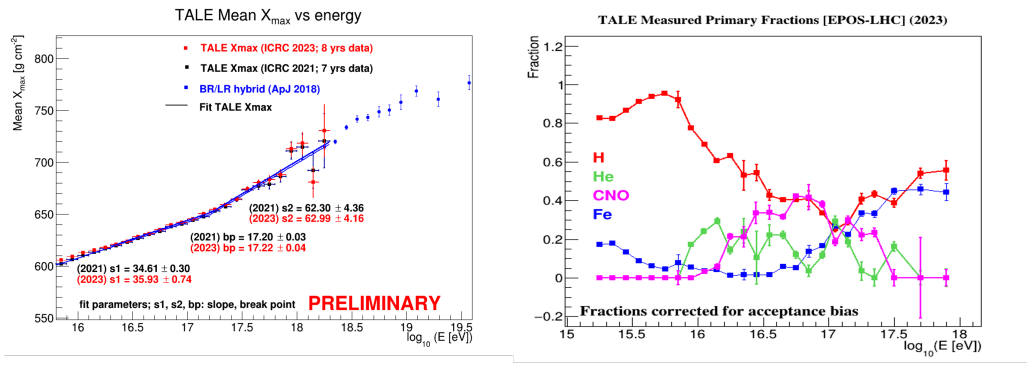


Figure 8: $\langle X_{\max} \rangle$ as a function of energy and primary cosmic ray fraction using 8 years of TALE FD monocular data [17]. **Left:** The red, black, and blue squares indicate the measured $\langle X_{\max} \rangle$ for 8 years, 7 years of TALE FD monocular data, and the TA hybrid data [22]. A change in the elongation rate $d\langle X_{\max} \rangle/d \log E$ occurs at $10^{17.2}$. **Right:** The fraction of four primary cosmic rays as a function of energy is presented with the red, green, magenta, and blue squares representing protons, helium, nitrogen, and iron, respectively. These results show a pattern of transitioning from light to heavy and back to light in the energy range of 10^{15} to 10^{18} eV.

3. Mass Composition

Here, we update the mass composition measurements from the TALE FD monocular and hybrid data, in the energy range from a few PeV to a few EeV. In addition, we report the results of ultra-high energy photon search using a neural network classifier.

The updated TALE FD mass composition analysis uses simulations of four primary species—proton, helium, nitrogen (CNO), and iron—using the EPOS-LHC hadronic model [17], whereas the TALE hybrid mass composition analysis simulates three primary cosmic ray particles—proton, nitrogen, and iron with the QGSJetII-04 model [21]. The Monte Carlo simulation data and real air showers registered in the detectors are processed using the same event selection and reconstruction procedures. The resulting shower X_{\max} distributions for each simulated primary type were used to fit the observed data X_{\max} distribution.

Figure 8 displays $\langle X_{\max} \rangle$ as a function of energy on the left and four primary cosmic ray fractions estimated by fitting the Monte Carlo distributions with the EPOS-LHC model on the right. This analysis uses 8 years of TALE FD monocular data [17]. In the left panel, the red squares represent the results of this analysis, while the blue data points at higher energies are obtained from a hybrid measurement conducted by TA [22]. The fitted line is in agreement with the $\langle X_{\max} \rangle$ values measured by the TA hybrid mode. A change in the elongation rate $d\langle X_{\max} \rangle/d \log E$ appears at energy $10^{17.2}$ eV, which can be interpreted as a change in the evolution of composition with energy. This change is likely correlated with the observed break in the cosmic ray energy spectrum [23]. The right panel shows the transition from light to heavy, and then back to light patterns in the energy range of 10^{15} eV to 10^{18} eV.

Figure 9 shows $\langle X_{\max} \rangle$ as a function of energy on the left and three primary cosmic ray fractions estimated by fitting Monte Carlo distributions with the QGSJetII-04 model on the right. For this analysis, we use 5 years of TALE hybrid data [21]. In the left panel, the black points represent $\langle X_{\max} \rangle$ values of the data, while the red, green, and blue colors indicate Monte Carlo rails of protons,

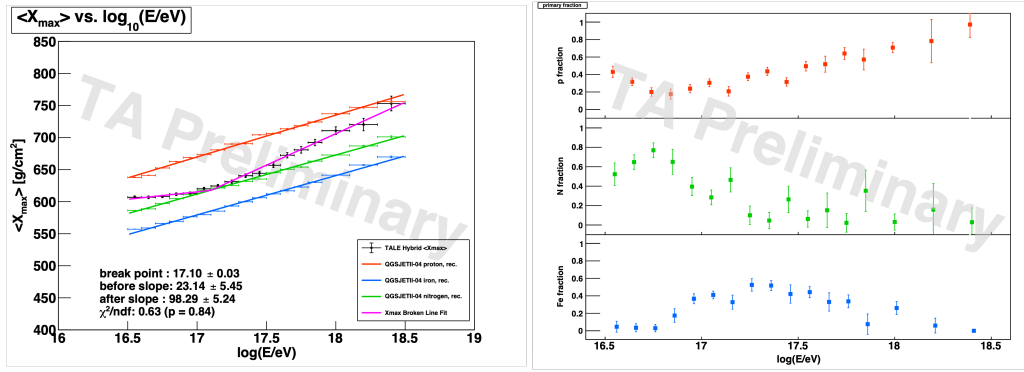


Figure 9: $\langle X_{\max} \rangle$ as a function of energy and primary cosmic ray fraction using 5 years of TALE hybrid data [21]. **Left:** The black points indicate $\langle X_{\max} \rangle$ values from the data, while the red, green, and blue points represent Monte Carlo simulations for protons, nitrogen, and iron, respectively. A change in the elongation rate $d\langle X_{\max} \rangle/d\log E$ appears $10^{17.1}$ eV. **Right:** The fraction of three primary cosmic rays as a function of energy is shown from top to bottom. The red, green, and blue squares denote protons, helium, nitrogen, and iron, respectively.

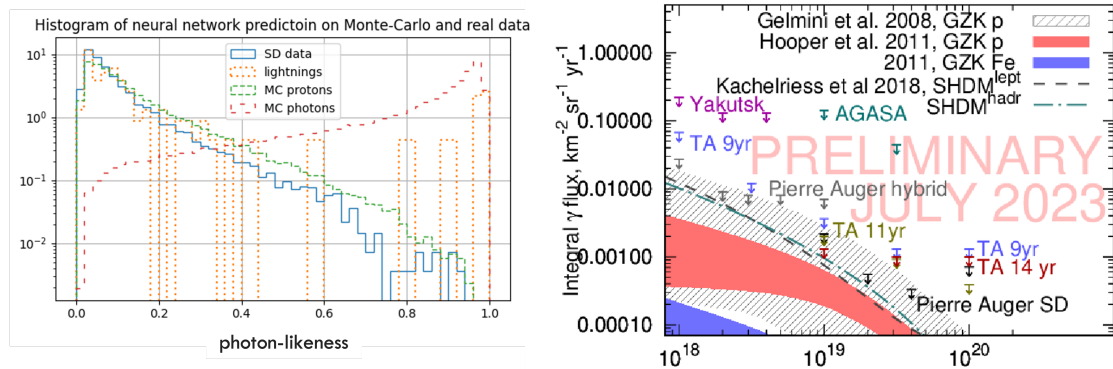


Figure 10: Comparison of the neural network predictions for SD data and photon flux limit estimation [24]. Left: The histograms show the neural network's predictions for SD data, lightning, and Monte Carlo proton- and photon-induced events. The x-axis indicates the photon-likeness, where 0 means a proton-like-induced air shower and 1 means a photon-like-induced air shower. This indicates that the neural network has successfully learned to identify photon-like-induced events. **Right:** Photon flux limits estimated using TA SD 14 years of data and our previous analysis results are shown alongside results from various collaborations. The red colors indicate the updated results, whereas the green and blue colors represent the previous 11-year and 9-year previous estimations, respectively.

nitrogen, and iron, respectively. This analysis shows a change in the elongation rate of $\langle X_{\max} \rangle$ at energy $10^{17.1}$ eV, which coincides with the 2nd knee in energy spectrum. The right panel shows the transition from light to heavy, and then back to light patterns in the energy range of $10^{16.5}$ eV to $10^{18.5}$ eV.

The TALE monocular and hybrid analyses yield consistent results regarding the break in the elongation rate and the estimation of the primary cosmic ray fraction. These results are consistent with a picture that the transition from galactic to extragalactic cosmic rays occurs over the ~ 1.5 decades of energy below the 2nd knee, which is approximately at 10^{17} eV.

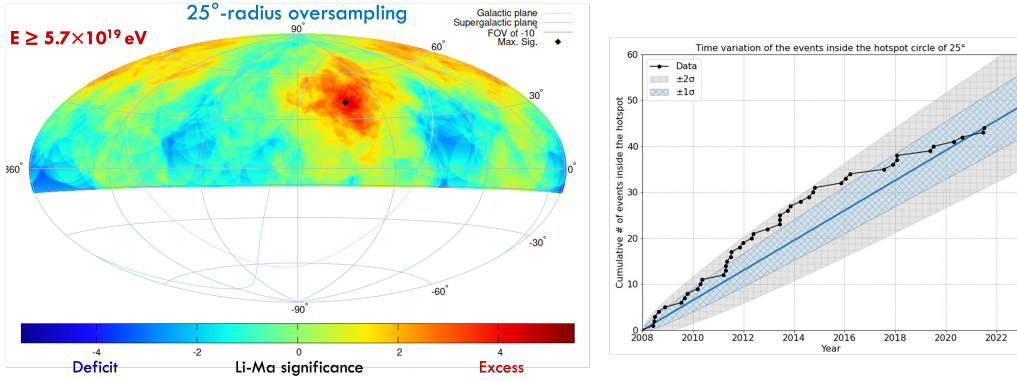


Figure 11: Sky map of the TA Hotspot in equatorial coordinates using a Hammer projection and its growth over the years [26]. **Left:** The color code represents the Li-Ma significance using a 25° -radius circle angular window in equatorial coordinates for 15 years of TA SD events with $E \geq 5.7 \times 10^{19}$ eV. The black diamond mark indicates the maximum Li-Ma significance at $(144.0^\circ, 40.5^\circ)$. **Right:** The black dots depict the cumulative number of events falling inside the Hotspot circle with a radius of 25° -radius circle at $(144.0^\circ, 40.5^\circ)$. The blue solid line indicates the estimated event rate inside the Hotspot. The light blue and gray bands represent $\pm 1\sigma$ and $\pm 2\sigma$ deviations from a linear increase rate.

We perform ultra-high energy photon searches using a neural network classifier to distinguish between protons and photons [24]. We train the neural network using TA SD reconstruction and test it with Monte Carlo datasets.

The left panel of Figure 10 shows a histogram of neural network prediction on Monte Carlo data and observed data. The x-axis indicates photon-likeness, where 0 means proton-like-induced air shower and 1 means photon-like-induced air shower. These histograms, plotted using a logarithmic scale for the vertical, clearly demonstrate that the neural network has effectively learned to identify photon-like-induced events. Based on this, we estimate the photon flux using 14 years of TA SD data. The results are shown in the right panel of Figure 10 on top of the analysis results of other collaborations. In this figure, the red points indicate the updated results, whereas the green and the blue represent the previous 11-year and 9-year estimations, respectively. Notably, the updated results are consistent with 11-year results [25].

4. Anisotropy

To investigate anisotropies in the arrival direction of UHECR, we perform oversampling searches using intermediate-scale angular circles and estimate the significances of excesses or deficits of events compared to the isotropic source Monte Carlo simulations. We report the updates on the intermediate-scale anisotropies—the TA Hotspot and the Perseus-Pisces supercluster (PPSC) excess—measured by the TA SD using the most up-to-date data, collected over 15 years [26].

The TA Hotspot refers to an excess of events with energies greater than 57 EeV, observed in the vicinity of the Ursa Major constellation. The left panel of Figure 11 shows the sky map of the Li-Ma significance using a 25° -radius circle angular window in equatorial coordinates. The color code indicates an excess (red) and a deficit (blue) of events compared to isotropy. The maximum

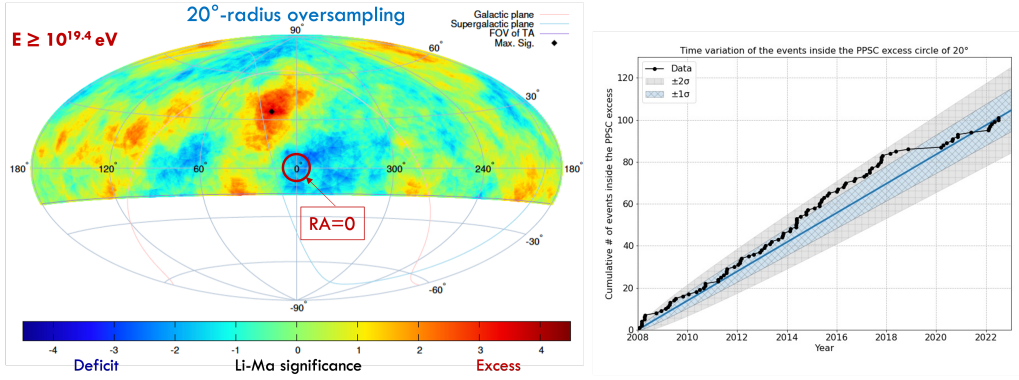


Figure 12: Sky map of the Perseus-Pisces supercluster excess in equatorial coordinates using a Hammer projection and its growth over the years [26]. **Left:** The Li-Ma significance maps are shown, using 20° -circle angular windows in equatorial coordinates for 15 years of TA SD events with energies greater than $10^{19.4}$ eV. Note that the coordinates are rotated by 180° in right ascension from Figure 11. The black diamond mark represents the positions of the maximum Li-Ma significance, located at $(17.9^\circ, 35.2^\circ)$. The excess overlaps with the Perseus-Pisces supercluster (PPSC) region. **Right:** The cumulative number of events observed inside the PPSC 20° -circle from $(17.9^\circ, 35.2^\circ)$ is shown with black dots. The blue solid line indicates the estimated event rate inside that circle. The light blue and gray bands represent $\pm 1\sigma$ and $\pm 2\sigma$ deviations from the linear increase rate, respectively.

Li-Ma significance is calculated to be 4.8σ at $(144.0^\circ, 40.5^\circ)$, marked by black diamond symbols, in equatorial coordinates.

To quantify how often such an excess appears anywhere in an isotropic UHECR sky within TA’s field of view by chance, we conduct a Monte Carlo study. The chance probability of finding such an excess is estimated to be 2.7×10^{-3} , approximately equivalent to 2.8σ . We also examine the growth of the Hotspot over the years. The increase rate of the events inside the Hotspot circle is consistent with the linear increase within $\sim 2\sigma$, as illustrated in the right panel of Figure 11.

The PPSC excess is an excess of events observed at slightly lower energies than those in the TA Hotspot. This intermediate-scale anisotropy in the arrival direction distributions was found during an investigation of the energy spectrum mismatch in the TA and Auger data. The energy range we examine is $10^{19.4}$ – $10^{19.6}$ eV, where the energy spectrum excess becomes prominent. The left panel of Figure 12 displays the sky map of the Li-Ma significance using a 20° -radius circle angular window in equatorial coordinates. The black diamond marks indicate the Li-Ma significances of 4.0σ at the position of $(17.9^\circ, 35.2^\circ)$ for $E \geq 10^{19.4}$ eV.

We also estimate the probability of having such an excess appearing in simulated isotropic UHECR sky by chance. For the evaluation of the PPSC excess, since the excess coincides with the overall distribution of the elements of the PPSC, we establish the criteria for the Monte Carlo study as follows. The positions of the maximum Li-Ma significances in the Monte Carlo datasets should be as close to the PPSC as the data. In other words, the Monte Carlo datasets should satisfy these criteria: $(S_{\text{mc}} \geq S_{\text{obs}})$ and $(\theta_{\text{mc}} \leq \theta_{\text{obs}})$. The chance probability of having an equal or higher excess as close to the PPSC as the data is estimated to be 3.3σ for $E \geq 10^{19.4}$ eV. Furthermore, we investigate the increase rate of the events inside the PPSC circle. The growth is consistent with the linear increase within $\sim 2\sigma$, as shown in the right panel of Figure 12.

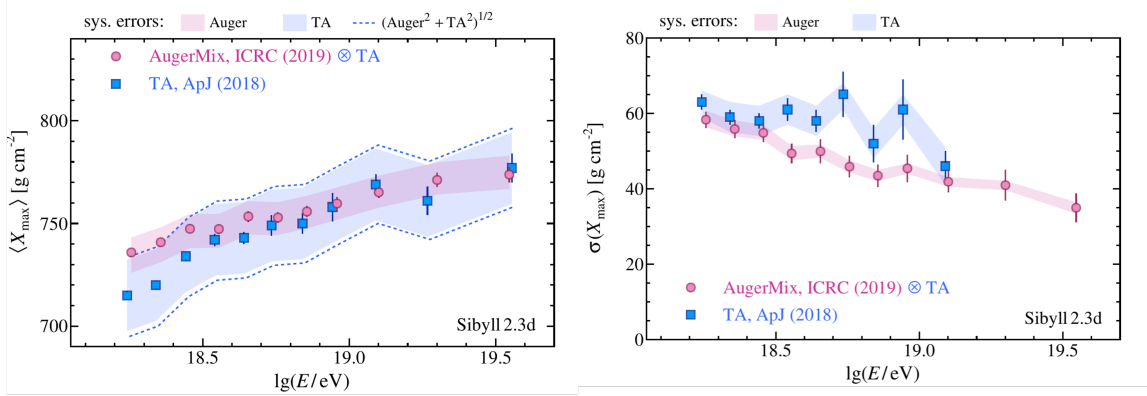


Figure 13: Comparison of $\langle X_{\max} \rangle$ (right) and $\sigma(X_{\max})$ (left) [27]. The measurements of $\langle X_{\max} \rangle$ at TA and for the Auger data transferred into the TA detector (AugerMix) using the Sibyll 2.3d high-energy interaction model are presented with the blue and red colors. The statistical and systematic errors of each are indicated with error bars and shaded areas, respectively. The dashed line in the left depicts Auger and TA systematic uncertainties combined in quadrature.

5. Joint and Interdisciplinary Research

TA and Auger have established collaborative working groups since 2012. These groups have engaged in detailed discussions regarding the technical aspects of data analysis methods concerning energy spectrum, mass composition, and anisotropy. Here, we present the results of the working groups' analyses related to mass composition [27] and anisotropies in arrival direction distributions [28, 29]. The analysis conducted by the spectrum working group is available separately [30, 31].

The composition working group employs a technique to transfer the best description of the Auger X_{\max} distributions in each energy bin to the TA detector simulation, event reconstruction, and analysis chain [27]. For this analysis, we use the Sibyll 2.3d hadronic interaction model. Figure 13 compares $\langle X_{\max} \rangle$ on the left and $\sigma(X_{\max})$ on the right. The results of $\langle X_{\max} \rangle$ are generally in agreement with statistical and systematic uncertainties. In the right figure, the X_{\max} fluctuations for the TA dataset, $\sigma(X_{\max})$, are not shown for $E > 10^{19.2}$ eV because of the challenges associated with reliably estimating it for these energy ranges, given the relatively limited event statistics. The measurements of TA and Auger are compatible at the current level of statistics and understanding of the systematics.

The anisotropy working group presents two analysis results: anisotropy searches and astrophysical interpretations using different source models, assuming various combinations of injected mass compositions and galactic and extragalactic magnetic field models [28, 29], as shown in Figure 14. The upper panels show that the cosmic ray flux map (left) and Li-Ma significance map (right) for the combined data of TA and Auger at $E_{\text{Auger}}^{\text{TA}} \geq \frac{48.2 \text{ EeV}}{38 \text{ EeV}}$, with a top-hat smoothing radius $\Psi = 25^\circ$ in equatorial coordinates. Three notable excesses are featured: one in the direction of the Centaurus constellation in the southern hemisphere, one near the direction of the Ursa Major constellation, and one in the direction of the Perseus-Pisces supercluster region [28].

The lower panels illustrate the results of likelihood analyses using various source models and injected mass compositions [29]. The left panel presents the result for the large-scale structure (LSS) source model using the 2MRS galaxy catalog [32], incorporating a composition mixture of

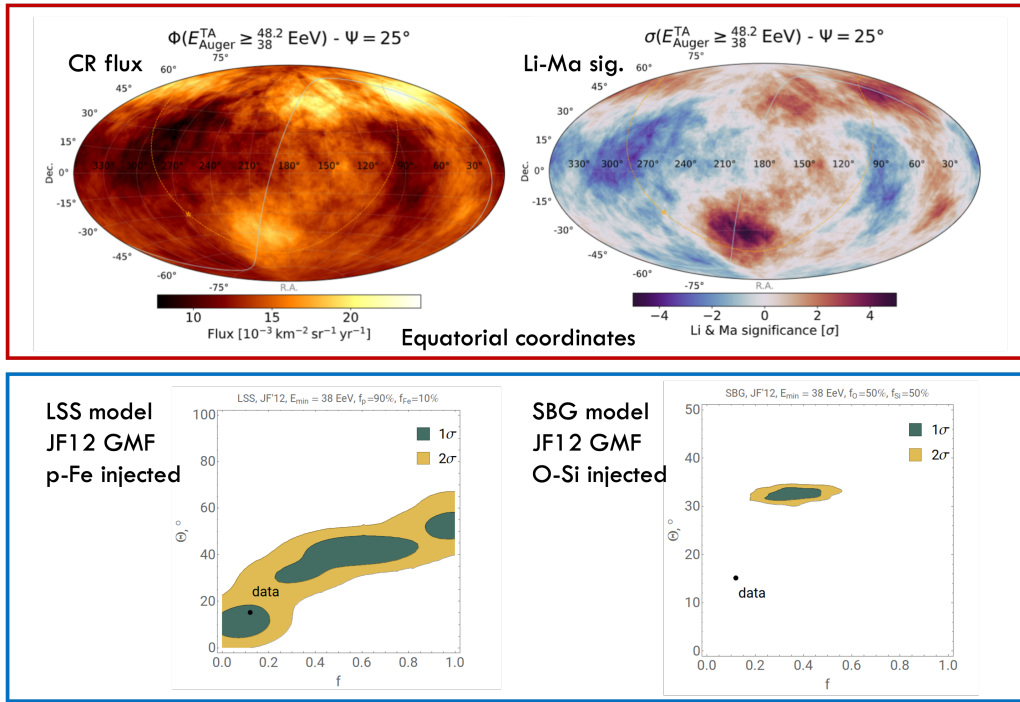


Figure 14: Results of joint observations of UHECR arrival directions using data recorded at the TA and Auger. Upper: The cosmic ray flux map (left) and Li-Ma significance map of combined data of TA and Auger at $E_{\text{Auger}}^{\text{TA}} \geq \frac{48.2}{38} \text{ EeV}$ with a top-hat smoothing radius $\Psi = 25^\circ$ in equatorial coordinates [28] (right). **Lower:** The results of the likelihood analysis using different source models and injected mass composition mixes [29].

90% protons and 10% iron. Alternatively, the right panel displays the results for the starburst galaxy (SBG) source model used in [33], incorporating a composition mixture of 50% oxygen and 50% silicon. These results serve as examples to demonstrate that some models are consistent with the data, while others are not. The former model results are consistent with the data between these two examples.

TA has collaborated with several interdisciplinary study groups, including those focused on thunderstorms, terrestrial gamma-ray flash (TGF), and imaging meteoroids. In this conference, we present observations of the optical emission of a lightning flash in conjunction with a downward-directed TGF at the TA SD [34]. For this work, TA constitutes a unique instrument that allows us to study gamma-ray emissions from the atmosphere over a very large area in conjunction with a radio-based lightning mapping array (LMA).

To investigate the optical emissions linked to a downward-directed TGF, we use the TA SDs along with a high-speed video camera, alongside various lightning measurement instruments positioned at the TA SD site. Figure 15 shows selected high-speed video frames of a lightning flash associated with a TGF and how the TA SDs collaborate to study the emission. This particular TGF resulted in a burst of three gamma-ray triggers reported by the TA SDs, which we referred to as triggers A, B, and C. The filled triangles in the right panel indicate the source height for each of these triggers. This analysis enhances our understanding of the initiation and propagation mechanism of TGF.

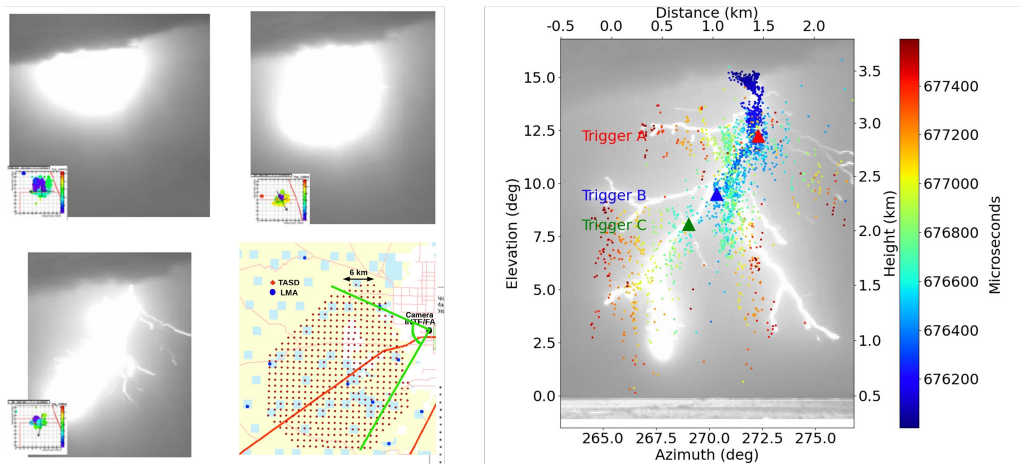


Figure 15: Optical emissions of a TGF and the map of TA SDs that detected the emission [34]. Left: Selected high-speed video frames of the TGF-producing flash are shown along with the map of TA SDs that triggered the emissions. **Right:** Plot of elevation vs. azimuth for the whole flash in a camera frame. The red, green, and blue triangles correspond to the sources of the TGF for triggers A, B, and C, as detected by the TA SDs consecutively.

6. Summary

In summary, the Telescope Array Collaboration has deployed and operated the TALE and TA×4 extensions and continued to run the original TA detectors to measure the properties of the EAS by employing a hybrid technique of utilizing arrays of scintillator detectors and fluorescence telescopes. Here, we included notable highlights from the presentations given by the Telescope Array Collaboration. More contributions are available in the proceedings of this conference.

Combining TALE+TA+TA×4 data, we measured over five orders of magnitude in energy, and six spectral features were detected: knee, low energy ankle, second knee, ankle, instep/shoulder feature, and cutoff. We found strong evidence of the spectrum anisotropy in the northern hemisphere (4.4σ global chance probability) near the cutoff energy. The mass composition analyses using TALE monocular and hybrid data revealed a light-heavy-light pattern in the energy range of 10^{15} – 10^{18} eV. It appears light and steady for $E > 10^{18}$ eV, but the statistics for energies greater than 10^{19} eV are not yet sufficient. By investigating the arrival direction distributions, we have identified two intermediate-scale anisotropies in data: a persistent TA Hotspot near the direction of the Ursa Major constellation and a new excess at slightly lower energy in the direction of the Perseus-Pisces supercluster. Looking ahead, we need to continue increasing statistics, particularly for the anisotropy and composition measurements. We aim to complete the TA×4 project and gather more data to further our understanding of cosmic rays.

References

- [1] Y. Tameda *et al.*, *PoS(ICRC2023)* **329** (2023).
- [2] S. Sakurai *et al.*, *PoS(ICRC2023)* **302** (2023).

- [3] F.W. Bradfield *et al.*, *PoS(ICRC2023)* **303** (2023).
- [4] Z.D. Plebaniak *et al.*, *PoS(ICRC2023)* **385** (2023).
- [5] F. Bisconti *et al.*, *PoS(ICRC2023)* **445** (2023).
- [6] M. Casolino *et al.*, *PoS(ICRC2023)* **208** (2023).
- [7] V. Kungel *et al.*, *PoS(ICRC2023)* **468** (2023).
- [8] T. Abu-Zayyad *et al.*, *Nuclear Instruments and Methods in Physics Research Section A-Accelerators Spectrometers Detectors and Associated Equipment*, **689**, 87 (2012).
- [9] H. Tokuno *et al.*, *Nuclear Instruments and Methods in Physics Research Section A-Accelerators Spectrometers Detectors and Associated Equipment*, **676**, 54 (2012).
- [10] R.U. Abbasi *et al.*, *Astrophysical Journal*, **865**, 74 (2018).
- [11] R.U. Abbasi *et al.*, *Nuclear Instruments and Methods in Physics Research Section A-Accelerators Spectrometers Detectors and Associated Equipment*, **1019**, 165726 (2021).
- [12] D. Heck, J. Knapp, J. Capdevielle, G. Schatz and T. Thouw, *Tech. Rep. FZKA 6019* (1998).
- [13] J. Kim *et al.*, *EPJ Web of Conferences* 02005 (2023).
- [14] A. Aab *et al.*, *Physical Review D* **102** 062005 (2020).
- [15] J. Hersil *et al.*, *Physical Review Letters* **6** 22 (1961).
- [16] K. Fujita *et al.*, *PoS(ICRC2023)* **400** (2023).
- [17] T. Abu-Zayyad *et al.*, *PoS(ICRC2023)* **379** (2023).
- [18] H. Oshima *et al.*, *PoS(ICRC2023)* **271** (2023).
- [19] K. Fujisue *et al.*, *PoS(ICRC2023)* **308** (2023).
- [20] T. Abu-Zayyad *et al.*, *Astroparticle Physics* **61** 93 (2015).
- [21] K. Fujita *et al.*, *PoS(ICRC2023)* **401** (2023).
- [22] R.U. Abbasi *et al.*, *Astrophysical Journal*, **858**, 76 (2018).
- [23] R.U. Abbasi *et al.*, *Astrophysical Journal*, **909**, 178 (2021).
- [24] I. Kharuk *et al.*, *PoS(ICRC2023)* **324** (2023).
- [25] O. E. Kalashev, *et al.*, *PoS(ICRC2021)* **864** (2021).
- [26] J. Kim *et al.*, *PoS(ICRC2023)* **244** (2023).
- [27] A. Yushkov *et al.*, *PoS(ICRC2023)* **249** (2023).

- [28] L. Caccianiga *et al.*, *PoS(ICRC2023)* (2023).
- [29] M. Kuznetsov *et al.*, *PoS(ICRC2023)* **528** (2023).
- [30] Y. Tsunesada *et al.*, *PoS(ICRC2023)* **406** (2023).
- [31] F. Salamida *et al.*, *PoS(ICRC2023)* **016** (2023).
- [32] J. P. Huchra *et al.*, *Astrophysical Journal Supplement Series* **199** 26 (2012).
- [33] J. Biteau *et al.*, *PoS(ICRC2021)* **307** (2021).
- [34] R. Abbasi *et al.*, *PoS(ICRC2023)* **250** (2023).

Full Authors List: Telescope Array Collaboration

R.U. Abbasi¹, Y. Abe², T. Abu-Zayyad^{1,3}, M. Allen³, Y. Arai⁴, R. Arimura⁴, E. Barcikowski³, J.W. Belz³, D.R. Bergman³, S.A. Blake³, I. Buckland³, B.G. Cheon⁵, M. Chikawa⁶, A. Fedynitch^{6,7}, T. Fujii^{4,8}, K. Fujisue⁶, K. Fujita⁶, R. Fujiwara⁴, M. Fukushima⁶, G. Furlich³, Z. Gerber³, N. Globus⁹, W. Hanlon³, N. Hayashida¹⁰, H. He⁹, R. Hibi², K. Hibino¹⁰, R. Higuchi⁹, K. Honda¹¹, D. Ikeda¹⁰, N. Inoue¹², T. Ishii¹¹, H. Ito⁹, D. Ivanov³, A. Iwasaki⁴, H.M. Jeong¹³, S. Jeong¹³, C.C.H. Jui³, K. Kadota¹⁴, F. Kakimoto¹⁰, O. Kalashev¹⁵, K. Kasahara¹⁶, S. Kasami¹⁷, S. Kawakami⁴, K. Kawata⁶, I. Kharuk¹⁵, E. Kido⁹, H.B. Kim⁵, J.H. Kim³, J.H. Kim^{3†}, S.W. Kim¹³, Y. Kimura⁴, I. Komae⁴, K. Komori¹⁷, Y. Kusumori¹⁷, M. Kuznetsov^{15,18}, Y.J. Kwon¹⁹, K.H. Lee⁵, M.J. Lee¹³, B. Lubsandorzhiiev¹⁵, J.P. Lundquist^{3,20}, T. Matsuyama⁴, J.A. Matthews³, J.N. Matthews³, R. Mayta⁴, K. Miyashita², K. Mizuno², M. Mori¹⁷, M. Murakami¹⁷, I. Myers³, S. Nagataki⁹, K. Nakai⁴, T. Nakamura²¹, E. Nishio¹⁷, T. Nonaka⁶, S. Ogio⁶, H. Ohoka⁶, N. Okazaki⁶, Y. Oku¹⁷, T. Okuda²², Y. Omura⁴, M. Onishi⁶, M. Ono⁹, A. Oshima²³, H. Oshima⁶, S. Ozawa²⁴, I.H. Park¹³, K.Y. Park⁵, M. Potts^{3‡}, M.S. Pshirkov^{15,25}, J. Remington³, D.C. Rodriguez³, C. Rott^{3,13}, G.I. Rubtsov¹⁵, D. Ryu²⁶, H. Sagawa⁶, R. Saito², N. Sakaki⁶, T. Sako⁶, N. Sakurai⁴, D. Sato², K. Sato⁴, S. Sato¹⁷, K. Sekino⁶, P.D. Shah³, N. Shibata¹⁷, T. Shibata⁶, J. Shikita⁴, H. Shimodaira⁶, B.K. Shin²⁶, H.S. Shin⁶, D. Shinto¹⁷, J.D. Smith³, P. Sokolsky³, B.T. Stokes³, T.A. Stroman³, Y. Takagi¹⁷, K. Takahashi⁶, M. Takamura²⁷, M. Takeda⁶, R. Takeishi⁶, A. Taketa²⁸, M. Takita⁶, Y. Tameda¹⁷, K. Tanaka²⁹, M. Tanaka³⁰, S.B. Thomas³, G.B. Thomson³, P. Tinyakov^{15,18}, I. Tkachev¹⁵, H. Tokuno³¹, T. Tomida², S. Troitsky¹⁵, R. Tsuda⁴, Y. Tsunesada^{4,8}, S. Udo¹⁰, F. Urban³², I.A. Vaiman¹⁵, D. Warren⁹, T. Wong³, K. Yamazaki²³, K. Yashiro²⁷, F. Yoshida¹⁷, Y. Zhezher^{6,15}, and Z. Zundel³

¹ Department of Physics, Loyola University Chicago, Chicago, Illinois 60660, USA

² Academic Assembly School of Science and Technology Institute of Engineering, Shinshu University, Nagano, Nagano 380-8554, Japan

³ High Energy Astrophysics Institute and Department of Physics and Astronomy, University of Utah, Salt Lake City, Utah 84112-0830, USA

⁴ Graduate School of Science, Osaka Metropolitan University, Sugimoto, Sumiyoshi, Osaka 558-8585, Japan

⁵ Department of Physics and The Research Institute of Natural Science, Hanyang University, Seongdong-gu, Seoul 426-791, Korea

⁶ Institute for Cosmic Ray Research, University of Tokyo, Kashiwa, Chiba 277-8582, Japan

⁷ Institute of Physics, Academia Sinica, Taipei City 115201, Taiwan

⁸ Nambu Yoichiro Institute of Theoretical and Experimental Physics, Osaka Metropolitan University, Sugimoto, Sumiyoshi, Osaka 558-8585, Japan

⁹ Astrophysical Big Bang Laboratory, RIKEN, Wako, Saitama 351-0198, Japan

¹⁰ Faculty of Engineering, Kanagawa University, Yokohama, Kanagawa 221-8686, Japan

¹¹ Interdisciplinary Graduate School of Medicine and Engineering, University of Yamanashi, Kofu, Yamanashi 400-8511, Japan

¹² The Graduate School of Science and Engineering, Saitama University, Saitama, Saitama 338-8570, Japan

¹³ Department of Physics, SungKyunKwan University, Jang-an-gu, Suwon 16419, Korea

¹⁴ Department of Physics, Tokyo City University, Setagaya-ku, Tokyo 158-8557, Japan

¹⁵ Institute for Nuclear Research of the Russian Academy of Sciences, Moscow 117312, Russia

¹⁶ Faculty of Systems Engineering and Science, Shibaura Institute of Technology, Minato-ku, Tokyo 337-8570, Japan

¹⁷ Graduate School of Engineering, Osaka Electro-Communication University, Neyagawa-shi, Osaka 572-8530, Japan

¹⁸ Service de Physique Théorique, Université Libre de Bruxelles, Brussels 1050, Belgium

¹⁹ Department of Physics, Yonsei University, Seodaemun-gu, Seoul 120-749, Korea

²⁰ Center for Astrophysics and Cosmology, University of Nova Gorica, Nova Gorica 5297, Slovenia

²¹ Faculty of Science, Kochi University, Kochi, Kochi 780-8520, Japan

²² Department of Physical Sciences, Ritsumeikan University, Kusatsu, Shiga 525-8577, Japan

²³ College of Science and Engineering, Chubu University, Kasugai, Aichi 487-8501, Japan

²⁴ Quantum ICT Advanced Development Center, National Institute for Information and Communications Technology, Koganei, Tokyo 184-8795, Japan

²⁵ Sternberg Astronomical Institute, Moscow M.V. Lomonosov State University, Moscow 119991, Russia

²⁶ Department of Physics, School of Natural Sciences, Ulsan National Institute of Science and Technology, UNIST-gil, Ulsan 689-798, Korea

²⁷ Department of Physics, Tokyo University of Science, Noda, Chiba 162-8601, Japan

²⁸ Earthquake Research Institute, University of Tokyo, Bunkyo-ku, Tokyo 277-8582, Japan

²⁹ Graduate School of Information Sciences, Hiroshima City University, Hiroshima, Hiroshima 731-3194, Japan

³⁰ Institute of Particle and Nuclear Studies, KEK, Tsukuba, Ibaraki 305-0801, Japan³¹ Graduate School of Science and Engineering, Tokyo Institute of Technology, Meguro, Tokyo 152-8550, Japan³² CEICO, Institute of Physics, Czech Academy of Sciences, Prague 182 21, Czech Republic

Acknowledgements

The Telescope Array experiment is supported by the Japan Society for the Promotion of Science(JSPS) through Grants-in-Aid for Priority Area 431, for Specially Promoted Research JP21000002, for Scientific Research (S) JP19104006, for Specially Promoted Research JP15H05693, for Scientific Research (S) JP19H05607, for Scientific Research (S) JP15H05741, for Science Research (A) JP18H03705, for Young Scientists (A) JPH26707011, and for Fostering Joint International Research (B) JP19KK0074, by the joint research program of the Institute for Cosmic Ray Research (ICRR), The University of Tokyo; by the Pioneering Program of RIKEN for the Evolution of Matter in the Universe (r-EMU); by the U.S. National Science Foundation awards PHY-1806797, PHY-2012934, PHY-2112904, PHY-2209583, and PHY-2209584 as well as AGS-1613260, AGS-1844306, and AGS-2112709; by the National Research Foundation of Korea (2017K1A4A3015188, 2020R1A2C1008230, & 2020R1A2C2102800); by the Ministry of Science and Higher Education of the Russian Federation under the contract 075-15-2020-778, IISN project No. 4.4501.18, by the Belgian Science Policy under IUAP VII/37 (ULB), by National Science Centre in Poland grant 2020/37/B/ST9/01821. This work was partially supported by the grants of the joint research program of the Institute for Space-Earth Environmental Research, Nagoya University and Inter-University Research Program of the Institute for Cosmic Ray Research of the University of Tokyo. The foundations of Dr. Ezekiel R. and Edna Wattis Dumke, Willard L. Eccles, and George S. and Dolores Doré Eccles all helped with generous donations. The State of Utah supported the project through its Economic Development Board, and the University of Utah through the Office of the Vice President for Research. The experimental site became available through the cooperation of the Utah School and Institutional Trust Lands Administration (SITLA), U.S. Bureau of Land Management (BLM), and the U.S. Air Force. We appreciate the assistance of the State of Utah and Fillmore offices of the BLM in crafting the Plan of Development for the site. We thank Patrick A. Shea who assisted the collaboration with much valuable advice and provided support for the collaboration's efforts. The people and the officials of Millard County, Utah have been a source of steadfast and warm support for our work which we greatly appreciate. We are indebted to the Millard County Road Department for their efforts to maintain and clear the roads which get us to our sites. We gratefully acknowledge the contribution from the technical staffs of our home institutions. An allocation of computing resources from the Center for High Performance Computing at the University of Utah as well as the Academia Sinica Grid Computing Center (ASGC) is gratefully acknowledged.

* Presently at: University of California - Santa Cruz

† Presently at: Argonne National Laboratory, Physics Division, Lemont, Illinois 60439,USA

‡ Presently at: Georgia Institute of Technology, Physics Department, Atlanta, Georgia 30332,USA